Strongly Nonlinear Superconducting Silicon Resonators

P. Bonnet,[1] F. Chiodi,[1,*] D. Flanigan●,[2] R. Delagrange,[1] N. Brochu,[1] D. Débarre,[1] and H. le Sueur[2,†]

[1]*Université Paris-Saclay, CNRS, Centre de Nanosciences et de Nanotechnologies, Palaiseau 91120, France*
[2]*Quantronics Group, Université Paris-Saclay, CEA, CNRS, SPEC, Gif-sur-Yvette 91191, France*

Superconducting boron-doped silicon is a promising material for integrated silicon quantum devices. In particular, its low electronic density and moderate disorder make it a suitable candidate for the fabrication of large inductances with low losses at microwave frequencies. We study experimentally the electrodynamics of superconducting silicon thin layers using coplanar waveguide resonators, focusing on the kinetic inductance, the internal losses, and the variation of these quantities with the resonator readout power. We report the observation in a doped semiconductor of microwave resonances with internal quality factors of a few thousand. As expected in the BCS framework, superconducting silicon presents a large sheet kinetic inductance in the 50–500-pH range, comparable to that of strongly disordered superconductors. The temperature dependence of the kinetic inductance is well described by the Mattis-Bardeen theory. However, we find an unexpectedly strong nonlinearity in the complex surface impedance that cannot be satisfactorily explained either by depairing or by quasiparticle heating.

I. INTRODUCTION

Lossless high-inductance microwave components made from superconducting materials are currently under intense study, both theoretically and experimentally, as they play a crucial role in cavity QED [1–3], in protecting qubits from their electromagnetic environment [4], in fast two-qubit gates [5], and in sensitive astronomical detectors [6–8]. The development of such components made from superconducting silicon would be of particular interest for silicon-based quantum electronics, which was initiated with the demonstration of CMOS silicon spin qubits [9]. Silicon becomes a superconductor when a few percent of the silicon atoms are replaced by boron [10]. Using a pulsed-laser-doping technique, layers of superconducting silicon ultradoped with boron (Si:B) can be fabricated with a controlled thickness and dopant concentration. This control allows one, in turn, to tune the superconducting critical temperature T_c in the 0–0.7-K range [11–13]. However, while the dc properties of such tunable BCS superconductor are now well understood, little is known about the surface impedance at the microwave frequencies that are relevant to applications in quantum information. The surface impedance of thin-film superconductors is often dominated by the kinetic inductance L_k, due to the inertia of the Cooper-pair condensate. L_k is proportional to the ratio of the normal-state sheet resistance $R_\square$ just above T_c to the superconducting gap energy Δ. Disordered superconductors and very thin films of elemental superconductors may have such a high $R_\square$ that the kinetic inductance strongly exceeds the "geometrical" inductance due to energy storage in the magnetic field.

Here, we report the observation in a superconducting doped semiconductor of microwave resonances with internal quality factors of a few thousand. We show that the kinetic inductance of our thin Si:B films is large, and comparable to that of strongly disordered superconductors such as TiN [14–16], NbN [17–19], NbTi [20], NbSi [21], W [22], and granular Al [23]. The measurements of the kinetic inductance of Si:B match predictions based on dc measurements of T_c and $R_\square$, where $R_\square/T_c$ is large due to the low carrier density and moderate disorder in the doped semiconductor. We show that the temperature and frequency dependence of the kinetic inductance also follows the predictions of the BCS-based Mattis-Bardeen equations. However, the nonlinearity, manifested by increases in both the kinetic inductance and the internal dissipation with increasing readout power, is unexpectedly large, and cannot be fully explained by either depairing [24] or quasiparticle heating [25].

II. EPITAXIAL SUPERCONDUCTING SILICON

Silicon strongly doped with boron is a type-II disordered BCS superconductor [10] with a critical temperature that increases with increasing boron concentration up to 0.7 K [13,27]. A nonequilibrium doping technique is necessary to create a superconductor because the minimum

---

*Corresponding author. francesca.chiodi@c2n.upsaclay.fr
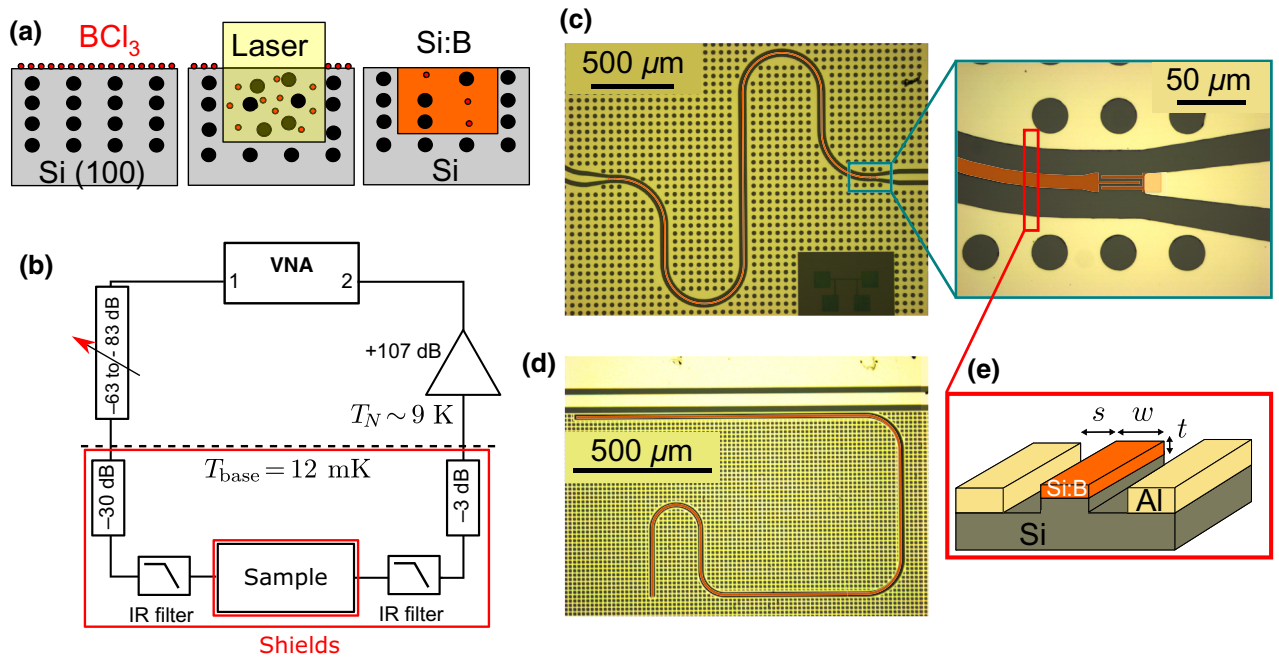†Corresponding author. helene.le-sueur@cea.fr

FIG. 1.   Fabrication, measurement, and design of Si:B resonators. (a) The steps in the gas-immersion laser-doping process. From left to right, chemisorption of the precursor gas BCl_3 onto the Si surface under ultrahigh-vacuum conditions; laser melting of the substrate by a 25-ns excimer laser pulse and boron diffusion throughout the liquid phase; and fast epitaxy of a superconducting Si:B crystal on the Si substrate. (b) Simplified cryogenic microwave setup. The sample is enclosed in a box made of either Au-plated Cu or superconducting Al, which, together with a global Cu shield on the base-temperature experimental stage, provides electromagnetic protection. The input line, on the left, is heavily attenuated and filtered so that we are able to probe the resonators down to the single-photon regime. On the base-temperature stage, we place homemade Eccosorb IR filters on both the input and the output of the sample, as well as either an attenuator (as shown here), a 4–8-GHz circulator, or a 3–12-GHz isolator on the output line to block thermal radiation from the input of the first-stage HEMT amplifier at 4 K. VNA, vector network analyzer. (c),(d) Optical micrographs of the two geometries of coplanar-waveguide (CPW) resonators used in the present work [26]. The Si:B sections are colored in orange. (c) Sample F, transmission type. (d) Sample C, shunt-coupled type. (e) Cross section of a CPW resonator. In both geometries, the connecting leads and the ground plane are made of Al, and the central conductor of the CPW is patterned in the Si:B layer, leaving the Si substrate in the gap between the Al and Si:B.

boron concentration required, $n_B \sim 3 \times 10^{20}$ cm^{-3} [13], is about 3 times the solubility limit [28]. For this purpose, we use gas-immersion laser doping (GILD) [26,29], whose principle is shown in Fig. 1(a) and discussed in the Appendix. The GILD technique turns the silicon substrate, over a thickness of 5–300 nm, into an epitaxial layer with a tunable boron concentration of up to 10 at. % (5×10^{21} cm^{-3}), without the formation of boron aggregates [30]. The layer is doped homogeneously through its thickness except for a metallic layer of few nanometers at the interface between the Si and Si:B, over which the doping drops to 0. The laser intensity has spatial inhomogeneities of approximately 1.5%, which result in spatial fluctuations of the layer thickness, and may also result in small fluctuations of the critical temperature.

The resonators described in this paper are patterned in Si:B layers grown epitaxially on a high-resistivity ($\rho > 3$ kΩ cm) Si substrate. These layers have a surface area of 2×2 mm, a thickness t from 23 to 35 nm, and a boron concentration from 4 to 4.7×10^{21} cm^{-3} (8 to 9.5 at. %).

The layers have a critical temperature T_c from 200 to 500 mK, a maximum transition width $\Delta T_c = 50$ mK, and a sheet resistance $R_\square$ from 30 to 80 Ω, corresponding to resistivities from 1×10^{-4} to 2×10^{-4} Ω cm. The layer thickness is much larger than the electronic mean free path $l_e \sim 5$ nm, and is comparable to or smaller than the superconducting coherence length $\xi \sim 50$–110 nm. These parameters, for all the resonators investigated here (labeled from A to I), are summarized in Table I together with their geometrical and electrical properties.

III. DESIGN AND FABRICATION OF SILICON RESONATOR

Our superconducting CPW resonators are fabricated as follows: first, the central conductor is patterned in the Si:B layer by optical lithography and a fluorine-based reactive ion etch, and then the ground planes and leads are patterned via liftoff from a 200-nm evaporated Al film. The ground-plane thickness is comparable to the etched depth around

TABLE I. Summary of the geometrical and electrical properties of the samples measured: thickness t, sheet resistance $R_\square$, critical temperature T_c, superconducting coherence length ξ, length and width of the Si:B central conductor of the CPW resonators, resonance mode, resonant frequency f_m, coupling quality factor Q_c, average low-power (typically below $\bar{n} = 100$) value of the internal quality factor Q_i, sheet kinetic inductance $L_{k,\square}$ extracted from the rf measurements, nonlinear coefficients K (Kerr coefficient) and γ, and their ratio (see text for details).

Sample	Thickness (nm) (± 5 nm)	$R_\square$ (Ω)	T_c (K)	ξ (nm) (± 5 nm)	Length (mm)	Width (μm)	Mode	f_r (GHz)	$10^{-3} Q_c$	Q_i	$L_{k,\square}$ (pH)	$-K/2\pi$ (s^{-1})	$\gamma_{\mathrm{NL}}/2\pi$ (s^{-1})	$-\gamma_{\mathrm{NL}}/K$
A ($\lambda/2$)	23	81	212	100	4.11	10	1	1.508	30.7	150	590 ± 30	$(1.1 \pm 0.13) \times 10^3$	550 ± 110	0.5
B ($\lambda/2$)	28	53	400	65	4.11	10	1	2.451	18.8	430	217 ± 15	-	-	-
E ($\lambda/2$)					4.75	10	1	3.264	46	1100	85 ± 2	$(3.5 \pm 0.4) \times 10^3$	1680 ± 245	0.48
							2	6.527	22.7	670		$(45 \pm 5) \times 10^3$	40050 ± 4950	0.89
F ($\lambda/2$)					4.10	10	1	3.482	7.3	3320	104 ± 0.5	300 ± 100	100 ± 15	0.34
							2	7.043	3.4	1950		2000 ± 200	1300 ± 140	0.65
							3	10.62	1.6	1280				
G ($\lambda/2$)	35	28	455	50	4.22	10	1	3.610	7.8	1750	91 ± 2	1010 ± 95	570 ± 100	0.56
H ($\lambda/2$)					4.22	10	1	3.630	34	950	91 ± 2	105 ± 20	60 ± 9	0.55
C ($\lambda/4$)					3.35	5	1	1.480	2.8	3920	90.3 ± 1.7	230 ± 70	30 ± 6	0.21
							3	4.356	6.0	1360		$(4.6 \pm 1.3) \times 10^3$	1800 ± 230	0.39
D ($\lambda/4$)					2.85	10	1	2.210	3.9	2630	90.9 ± 1.4	170 ± 40	40 ± 9	0.25
							3	6.529	2.7	1140		$(12.3 \pm 1.8) \times 10^3$	8120 ± 1350	0.66
I ($\lambda/4$)					3.9	50	1	2.830	1.9	350	93 ± 1	$(2.5 \pm 0.6) \times 10^3$	3250 ± 2000	1.3

the Si:B line. The use of Al allows us (i) to keep a constant impedance matching of our samples to the microwave equipment regardless of the surface impedance of the Si:B, and (ii) to simplify the system under study to a single conductor, allowing more accurate extraction of the kinetic inductance value [31]. The Al ground plane in the vicinity of the resonator contains a grid of 10-μm-wide holes, acting as magnetic flux traps to limit the dissipation due to vortex motion [32] [Figs. 1(c) and 1(d)].

We characterize both half-wave ($\lambda/2$) and quarter-wave ($\lambda/4$) resonators. The half-wave resonators are coupled at both ends to on-chip 50-Ω Al transmission lines via small capacitances. These resonators are measured in a transmission configuration: the measured signal propagates through the resonator [Fig. 1(c)]. The quarter-wave resonators are coupled at their open end to a 50-Ω transmission line, while their opposite end is shorted to the Al ground plane. These resonators are measured in a shunt configuration, meaning that the measured signal is the complex sum of the signal propagating past the resonator and the signal radiated from it in the forward direction [Fig. 1(d)]. The latter geometry is best suited for reading out several resonators with different resonance frequencies in a single run. In our samples, the transmission line crosses three laser-doped spots, each containing one resonator. Four-wire dc measurements are performed in parallel on laser-doped samples fabricated at the same time.

The design of the resonators is determined by adjusting the resonance frequencies f_r and coupling loss rates κ_c with microwave simulations in the SONNET software package (see Appendix). To achieve an accurate determination of the resonators' internal loss rates κ_i, we target values of the coupling losses κ_c near the critical coupling $\kappa_c \sim \kappa_i$. κ_c is in the range 3–150×10^5 s^{-1}, corresponding to quality factors $Q_c = 2\pi f_r/\kappa_c \sim 2000$–$46\,000$, while $\kappa_i \sim 20$–600×10^5 s^{-1} corresponds to quality factors $Q_i = 2\pi f_r/\kappa_i \sim 150$–$4000$ (see Table I).

IV. MEASUREMENT SETUP AND LINEAR RESPONSE

We use conventional microwave spectroscopy measurements of the superconducting Si:B resonators to determine the kinetic inductance of the film, the internal loss rates κ_i of the resonators, and the amount of nonlinearity in both of these quantities. We extract these values from measurements of the complex forward-scattering parameter S_{21} at frequencies from 1 to 12 GHz, at temperatures from 12 to 350 mK, and using power levels P_{in} at the sample input that range from -145 to -90 dBm. At resonance, the photon number in the resonator is $\bar{n} = P_{\mathrm{in}}2\kappa_c/\hbar\omega_r\kappa_t^2$, where $\kappa_t = \kappa_c + \kappa_i$ is the total loss rate; this photon number varies from less than 1 to a few million for the power levels used here. As shown in Fig. 1(b), both the input and the

output lines are shielded to prevent the resonators being significantly populated with thermal photons. In the output, between the sample and the HEMT, either a -3-dB attenuator (to enable wideband measurements) or a 3–12-GHz isolator is inserted. With the -3-dB attenuator, in the worst-case scenario, for sample C, which has the lowest resonance frequency and the highest quality factor, the estimated thermal population is about $\bar{n}_{th} = 8$ photons in the fundamental, and drops to $\bar{n}_{th} = 0.7$ in mode 3.

The measured S_{21} is the product of the signal of interest transmitted through the chip and the background transmission due to the input and output lines. In the shunt configuration, the background transmission can be measured for the normal state of the Si:B, while the Al is in the superconducting state. This compromise is best achieved around 400 mK, where no Si:B resonance can be detected, and where the background transmission is almost independent

of the temperature. In the transmission configuration, the background is estimated in a separate run. With this background removed, the transmission coefficient used to fit the data in the shunt configuration is

$$S_{21} = 1 - (1 + iA)\frac{\kappa_c}{\kappa_c + \kappa_i + 2i\delta\omega}, \qquad (1)$$

while that for the transmission configuration is

$$S_{21} = S_L + \frac{2\kappa_c}{2\kappa_c + \kappa_i + 2i\delta\omega}, \qquad (2)$$

where $\delta\omega = 2\pi(f - f_r)$ is the detuning. The asymmetry A and leakage S_L account for on-chip imperfections: A is nonzero when the field radiated from the resonator is reflected off an impedance mismatch such as that occurring at the microbonding connections [33,34], while S_L is
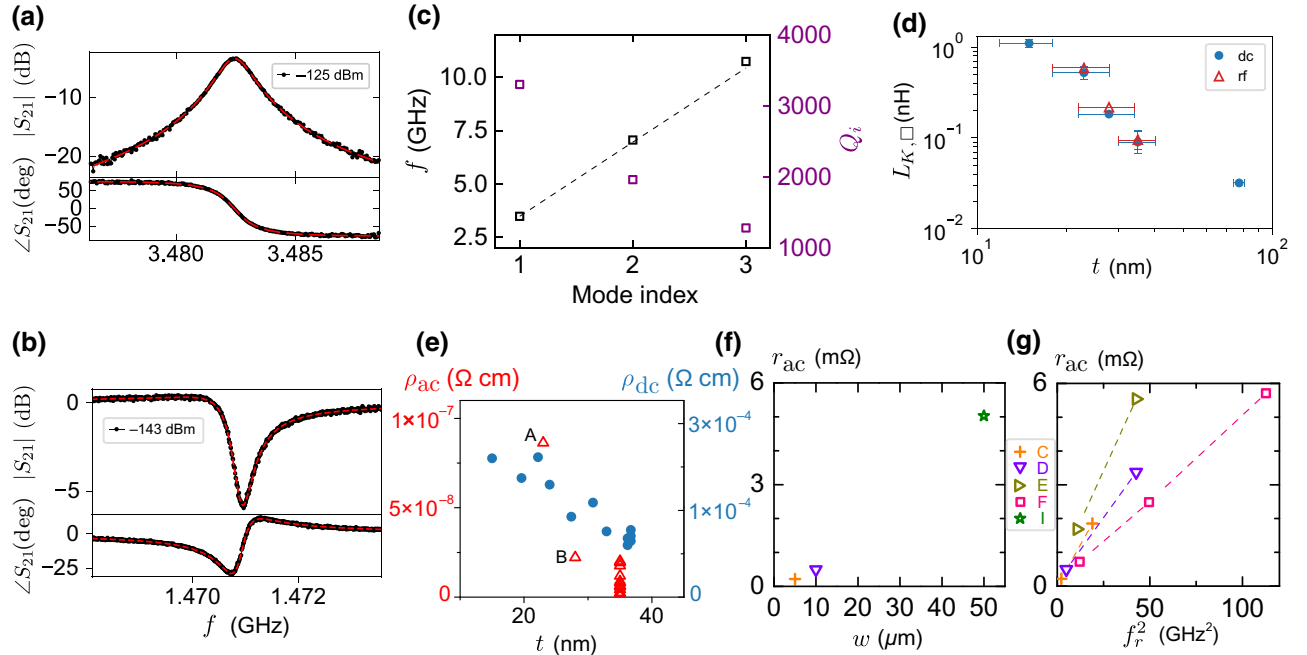

FIG. 2.　Linear properties of Si:B in the microwave domain. (a) Typical data for scattering parameter S_{21} as a function of frequency f across a resonance (black dots) in the transmission-coupled geometry with the background transmission of the setup removed. The data are taken from sample F at a temperature $T = 14$ mK and readout power $P = -125$ dBm. The red dashed line fits of Eq. (2) to the data [26]. (b) As (a), for the shunt-coupled geometry. The data are taken from sample C, with $T = 11$ mK and $P = -143$ dBm. The red dashed line fits of Eq. (1) [26]. The distortion of the curves is not related to nonlinear effects, but is due to impedance mismatch, modeled by the asymmetry parameter A in Eq. (1). (c) Resonance frequency and quality factor of the first three modes of sample F (half-wave) measured at $T = 14$ mK. The black dashed line follows $f_m = mf_1$, where m is the mode index. The internal quality factor is always found to decrease with increasing frequency for a given device. (d)–(g) Kinetic inductance and losses. Summary of the main rf figures gathered together in Table I for all samples measured in the present work. (d) Sheet kinetic inductance $L_{k,\square}$ as a function of Si:B thickness, inferred from measurements at dc (blue dots) or at rf (red triangles). The error bars attributed to the thickness are associated with the uncertainty in the thickness of the superconducting layer within the doped layer. When plotted, the error bars on $L_{k,\square}$ correspond to a statistical error obtained from several samples. The individual error in the extraction of $L_{k,\square}$ is smaller than the symbol width. (e) The ac sheet resistivity (red triangles, left axis) ρ_{ac} is found to decrease with increasing thickness, and follows the same trend as the dc resistivity (blue dots, right axis) measured independently. (f) The ac sheet resistance r_{ac} increases with the width of the Si:B central conductor; (g) it increases quadratically with frequency. Each symbol represents a resonator. Resonators C, D, and I are nominally identical Si:B layers, processed and measured simultaneously on the same chip. (g) shows exclusively the samples where both the fundamental and one or two harmonics are measured.

nonzero when the input signal is coupled directly to the output.

The linear response is measured with a minimum applied power corresponding to a few photons on average in the resonator, where the curve $S_{21}(f)$ is independent of the readout power. The experimental data are fitted with Eq. (1) or (2) up to 350 mK, where most resonances vanish in the noise. From these fits, we extract f_r, κ_i, and κ_c as functions of temperature up to $T \sim 0.6 T_c$. Characteristic measurements together with the corresponding fits are presented in Figs. 2(a) and 2(b). As expected, our resonators are multimodal, with resonant frequencies scaling with the mode number m as $f_m = m f_1$ for half-wave resonators and as $f_m = (2m - 1)f_1$ for quarter-wave resonators. In our experimentally accessible frequency range, we can thus observe the first two or three modes of each resonance.

V. LOW-TEMPERATURE KINETIC INDUCTANCE IN THE LINEAR REGIME

In the BCS theory, the kinetic inductance at low temperature ($T \ll T_c$) and low frequency ($hf \ll 2\Delta$) is

$$L_k = \frac{\hbar R_\square}{\pi \Delta} \frac{1}{\tanh(\Delta / 2k_B T)}. \quad (3)$$

In the case where the inductance is so high that the current density is uniform, it is convenient to introduce the sheet kinetic inductance $L_{k,\square}$, as is done for the sheet resistance. This quantity is relevant in our experiments, where only the central conductor of the CPW resonator is made from Si:B, and has a small cross section.

Using Eq. (3) with the sheet resistance $R_{N,\square}$ and T_c extracted from dc measurements, $L_{k,\square}$ is found to be in the range from 50 to 470 pH/$\square$ for Si:B thicknesses ranging from 20 to 80 nm. These values are then compared with those extracted from the rf measurements by adjusting the SONNET electromagnetic simulations to reproduce the measured resonance frequencies. Note that the $L_{k,\square}$ values deduced from the SONNET simulations are found to be in good agreement with the analytical values obtained from the resonant frequency $f_1 = 1/pl\sqrt{\mathcal{C}_g(\mathcal{L}_g + \mathcal{L}_k)}$ for the first mode, where l is the length of the resonator, $p = 2$ (4) for a $\lambda/2$ ($\lambda/4$) resonator, and $\mathcal{C}_g$, $\mathcal{L}_g$, and $\mathcal{L}_k$ are the capacitance, geometric inductance, and kinetic inductance, respectively, per unit length. This expression, where the current distribution (relatively homogeneous) across the width of the central conductor is taken into account (see Appendix), is valid when the losses can be neglected. Figure 2(d) shows excellent agreement between the $L_{k,\square}$ values inferred from the high-frequency measurements and those calculated from the dc characteristics, confirming the validity of the BCS description and suggesting that values of the order of 1 nH/$\square$ could be obtained in Si:B resonators patterned from thinner layers. For all

our samples, the kinetic inductance participation ratio $\alpha = L_k/(L_k + L_g)$ ranges from 0.94 to 0.99. The characteristic impedance of the resonators, $Z_r = \sqrt{\mathcal{L}_{\text{tot}}/\mathcal{C}_g}$, lies in the range from 150 to 700 Ω. In particular, the 35-nm-thick resonators, whose results are mainly shown here, have $Z_r \sim (300\text{--}380)$ Ω.

VI. LOW-TEMPERATURE LOSSES IN THE LINEAR REGIME

Noticeably, the measured internal losses do not depend on the power within the error bars of the fit at low occupation numbers (typically below $\bar{n} = 100$ photons). In particular, we can never observe in the Si:B samples the characteristic power dependence of Q_i due to two-level systems (TLS) [35], since the dominant loss mechanism is much more prominent. The single-photon TLS loss rate measured for aluminum resonators with similar CPW geometries and fabrication recipes is in fact 2–3 orders of magnitude smaller. From now on, the quoted values for Q_i in the linear regime are the average values of the fit results at low occupation numbers $\bar{n} \lesssim 100$.

To dig into the origin of the observed microwave losses, we evaluate the residual resistance at microwave frequencies in the Si:B layer with an effective *RLC* lumped-element model of the resonator. As with the extraction of the sheet kinetic inductance from the resonance frequency, we aim at extracting the residual sheet resistance from the losses, describing our material independently of the device geometry. We compute the ac sheet resistance from the internal quality factor and the sheet kinetic inductance with $r_{\text{ac}} = \omega_r L_{k,\square}/\alpha Q_{i,\text{sat}}$, where $Q_{i,\text{sat}}$ is the low-temperature value of the internal quality factor of the mode [typically below $T_c/10$; see Fig. 3(b)]. This sheet resistance is reflective of the Ohmic losses in the inductor and ranges from 0.2 to 40 mΩ/$\square$. We find that the ac losses depend on the layer thickness, as already observed for the dc resistivity [Fig. 2(e)]: when the thickness decreases, both the ac and the dc Si:B resistivities ($\rho_{\text{ac}} = r_{\text{ac}}t$; $\rho_{dc} = R_\square t$) increase as a result of a larger amount of interstitial boron and, correspondingly, of disorder [36] (see Appendix). The highest values of r_{ac} are observed for the thinner, lossier, and more disordered samples, which present the highest $L_{k,\square}$. Furthermore, r_{ac} increases strongly with the resonator width, as observed in Fig. 2(f) for samples C, D, and I, whose laser doping and fabrication are performed at the same time, and which are probed by the same transmission line. Finally, r_{ac} is plotted against frequency in Fig. 2(g) for the samples where multiple harmonics can be measured, and is shown to increase as f_r^2. The frequency and width dependences are in quantitative agreement with ac losses due to magnetic vortices, in which the motion of the nonsuperconducting vortex cores leads to dissipation (see Appendix). However, in a control experiment with extensive magnetic shielding on sample C, the losses are not found to
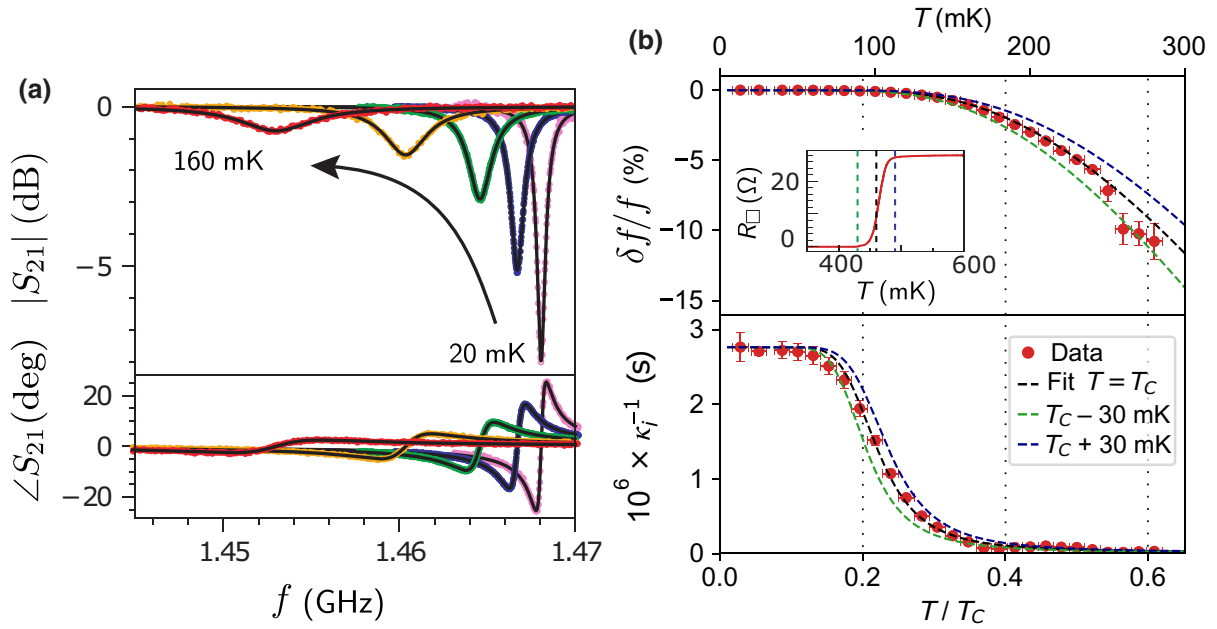
FIG. 3. Evolution of one resonance with temperature for sample C obtained in several cooldowns, and comparison with the Mattis-Bardeen theory. (a) $S_{21}(f)$ data (dots) from 20 to 160 mK after removal of the reference background taken at 400 mK, compared with fits of Eq. (1) (black lines). (b) Relative frequency shift and inverse internal losses as a function of temperature expressed in reduced units of T_c. The black dashed line is the Mattis-Bardeen prediction using the measured T_c, with no free parameters. The colored dashed lines are fits using $T_c \pm 30$ mK. Inset: four-wire dc measurements of the sheet resistance $R_\square$ of the same Si:B layer, showing $T_c = 460 \pm 30$ mK and $R_\square = 28\,\Omega$ in the normal state just above T_c.

vary significantly. This could indicate that another type of vortex loss, involving vortex-antivortex pairs, is at play. Other features can also contribute to the observed losses. For instance, a metallic layer a few nanometers thick is present at the Si:B/Si interface, where the dopant concentration decreases below the superconductivity threshold, and whose thickness depends on the layer properties. However, the associated ac sheet resistance is not expected to depend on the conductor width. Further experiments are still needed to discriminate between the possible sources of loss.

VII. TEMPERATURE DEPENDENCE OF RESONANT FREQUENCY AND LOSSES—MATTIS-BARDEEN THEORY

Figure 3(a) shows a selection of the background-removed S_{21} data measured in the linear-response regime at several temperatures for sample C. A reduction of the resonant frequency and quality factor is observed, as the thermally induced Cooper-pair breaking increases the kinetic inductance and the losses [31]. In Fig. 3(b), we compare the characteristic temperature dependence of the relative frequency shift $\delta f/f$ and the inverse internal losses $\kappa_i^{-1} = Q_i/\omega$ with the predictions of the Mattis-Bardeen theory [37], which is valid for homogeneous weakly coupled BCS superconductors with low

or moderate disorder. The evaluation of the frequency-dependent complex conductivity is based on two input parameters extracted from dc measurements: T_c and $R_\square$. Figure 3(b) shows the good agreement obtained for the frequency shift, without any free parameters, up to temperatures as high as $0.6T_c$, where $\delta f/f$ decreases by 10%. We add to Fig. 3(b), to guide the eye, the Mattis-Bardeen expectations for $T_c + 30$ mK and $T_c - 30$ mK. Such a temperature range corresponds roughly to the width of the superconducting transition of the sample, as shown in the inset of Fig. 3(b). Above $0.6T_c$, the determination of $\delta f/f$ and κ_i becomes increasingly difficult due to the vanishing amplitude of the field coming out of the resonator (since $\kappa_c \ll \kappa_i$), and to the low readout power required to remain in the linear regime. Despite the increased uncertainty, however, a small shift from the expected dependence can be observed above $0.55T_c$. This may be the result of some inhomogeneities in Δ in the Si:B layer, as a gap dispersion of the order of $\pm 10\%$ has been measured by scanning tunneling spectroscopy [27].

Figure 3(b) shows the temperature dependence of the internal losses. At high temperatures ($T > 0.3T_c$), the losses due to thermally activated quasiparticles are well described by the Mattis-Bardeen theory ($\kappa_i \sim \kappa_{\mathrm{MB}}$). At the base temperature, κ_i is found to saturate due to additional loss mechanisms, giving a saturation value κ_{sat}. The total internal losses are written $\kappa_i(T) = \kappa_{\mathrm{MB}}(T) + \kappa_{\mathrm{sat}}$.

The saturation value takes into account all the usual nonthermal contributions, such as quasiparticles excited by unshielded radiation or by the readout power, and dissipation due to TLS or vortex motion. In conclusion, the linear response of Si:B at finite frequencies shows good agreement with the BCS-based Mattis-Bardeen theory at all temperatures for the purely reactive (inductive) response. At temperatures $T < 0.2T_c$, however, a loss mechanism, discussed when we comment on the ac sheet resistance at the base temperature, takes over the dissipative response.

VIII. NONLINEARITIES IN KINETIC INDUCTANCE AND LOSSES

The results shown up to now are characteristic of the linear regime. However, when the readout power is increased, the resonances shift towards low frequencies and then become progressively skewed, up to a bistable state where hysteresis is observed between frequency sweeps up and down [Fig. 4(a)]. Along with this change in resonance frequency and shape, we also note an increase in the internal losses, with a reduction of the resonance amplitude. From a qualitative point of view, this nonlinearity appears in Si:B at an extremely low power: as an example, the first mode ($f_1 = 1.48$ GHz) of sample C undergoes frequency shifts of the order of 100 kHz at readout powers of the order of femtowatts, corresponding to about 200 photons in the resonator, while the hysteresis appears at picowatt powers. To describe quantitatively the resonance curves in the nonlinear regime, the harmonic-oscillator Hamiltonian characteristic of the linear regime is replaced by $H = \hbar\omega_r a^\dagger a + (\hbar/2)K a^\dagger a^\dagger a a$, where $a^\dagger$ and a are the photon creation and annihilation operators, and K is the Kerr

coefficient, quantifying the nonlinear response. The energies of this oscillator are no longer equidistant, but acquire a Fock-state-dependent shift $(E_{n+1} - E_n)/\hbar = \omega_r + nK$, where n is the Fock index. In consequence, the measured resonance shifts with respect to the average photon population $\bar{n}$ can be written as $\omega_r^{\mathrm{NL}} = \omega_r + \bar{n}K$ [38]. Nonlinear losses can also be taken into account, by introducing a loss term proportional to the number of photons and write the total losses as $\kappa_{\mathrm{tot}}^{\mathrm{NL}} = \kappa_c + \kappa_i + \bar{n}\gamma$. The transmission coefficient, in the case of a shunt-coupled geometry, finally reads

$$S_{21}^{\mathrm{NL}} = 1 - \frac{(1 + iA)\kappa_c}{(\kappa_c + \kappa_i + \bar{n}\gamma) + 2i[\omega - (\omega_r + \bar{n}K)]}. \quad (4)$$

A similar expression is found for the transmission geometry. Figure 4(b) shows the results of the fits obtained from Eq. (4), where the curves in the low-power range, for both the up and the down sweeps, are described by a single Kerr number K and a single nonlinear loss term γ. The other parameters in the fit, κ_c, κ_i, f_r, and the asymmetry A, are fixed at their linear-regime values. All the curves measured in the wider power range, corresponding to $\bar{n} = 1$–10^4 photons in the resonators, are well described by Eq. (4), but only the low-power curves, with $\bar{n} \lesssim 1000$, can be described by a common K and γ. This deviation may be due to higher-order terms in the Hamiltonian. Henceforth, we discuss exclusively the low-power nonlinear parameters. Note that the low-power Kerr values and nonlinear losses deduced from the nonlinear fit are in good agreement, within 20%, with the linear variation with $\bar{n}$ of the resonant frequency and losses extracted from linear fits of $|S_{21}(f)|$ for $\bar{n} \lesssim 500$ [see Fig. 4(c)].
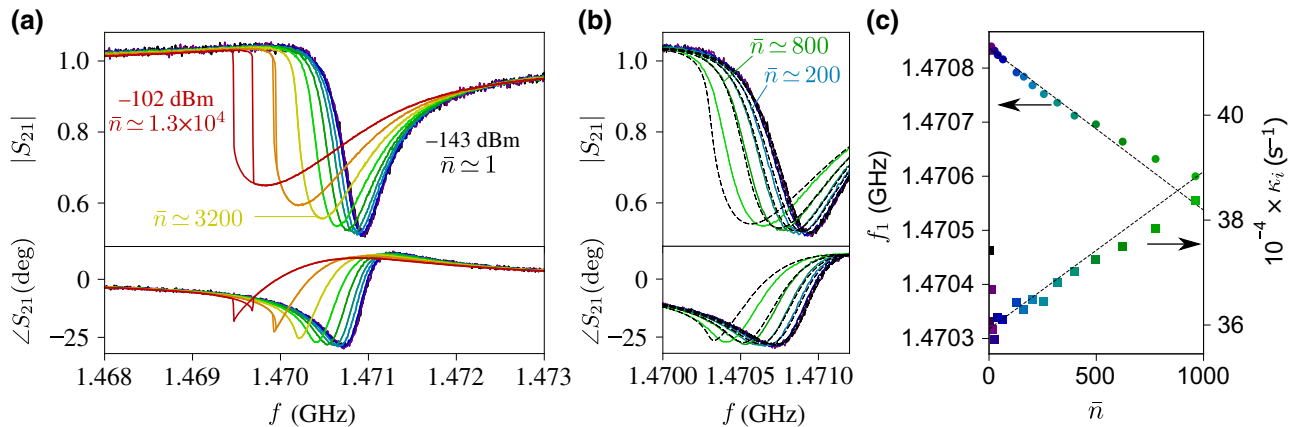

FIG. 4.   Measurement and fit of the nonlinear scattering parameters of sample C. (a) Evolution of the resonance with increasing input power for the first mode at $T = 14$ mK. (b) A low-power subset of the measured values of S_{21} is fitted with Eq. (4) (dashed lines) for common values of $K_{\mathrm{low}}/2\pi = -300$ s^{-1} and $\gamma_{\mathrm{low}}/2\pi = 30$ s^{-1}. (c) For the same subset, the apparent resonance frequency (dots) and internal losses (squares) are deduced from the position and amplitude of the dip in $|S_{21}(f)|$, and are plotted against the average photon number $\bar{n}$. The symbol color encodes the input power on the same scale as in (a),(b). The dashed lines correspond to the same K and γ as those of the complete fits: $\partial f_1/\partial\bar{n} = K_{\mathrm{low}}/2\pi$ and $\partial\kappa_i/\partial\bar{n} = \gamma_{\mathrm{low}}$.
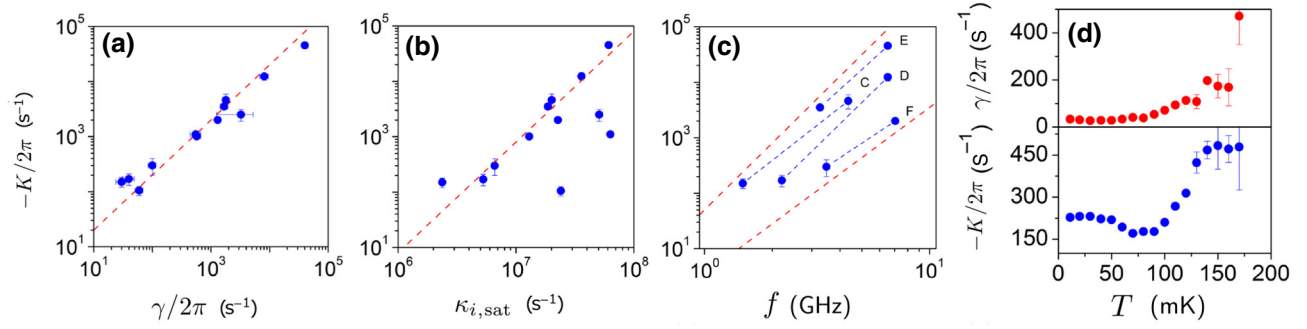
FIG. 5. General trends in the nonlinearity in Si:B. (a) Reactive versus dissipative nonlinearity for all the samples reported in Table I: Kerr coefficient versus nonlinear losses γ. The dashed line corresponds to $\gamma/K = 0.5$. (b) Kerr coefficient versus linear losses at the base temperature (20 mK) for all the samples reported in Table I. The dashed line corresponds to $K \propto \kappa_{i,\text{sat}}^2$. (c) Kerr coefficient versus frequency for samples where the nonlinearity is measured for multiple harmonics. The dashed lines (shifted for clarity) correspond to $K \propto f^3$ and $K \propto f^4$. (d) Kerr coefficient and nonlinear losses versus temperature for sample C. The labels correspond to those in Table I. The decrease in the Kerr coefficient between 20 and 60 mK may be associated with heating (see discussion in Sec. X).

The extracted $K/2\pi$ and $\gamma/2\pi$ are reported in Table I for the measured harmonics of all resonators. The fits output a negative K and a positive γ, consistent with the expectation that, whatever the nonlinearity mechanism, it corresponds to a weakening of superconductivity and thus an increase in the kinetic inductance and additional losses in the system. The smallest Kerr numbers reported are, in absolute value, of the order of 100 Hz/photon for macroscopic CPW structures, showing the extreme sensitivity of superconducting silicon to microwave power. In Fig. 5, we plot the variation of the Kerr coefficient against the nonlinear losses γ, the saturation losses in the linear regime $\kappa_{i,\text{sat}}$, the frequency, and the temperature. The nonlinear inductive response (K) is associated with nonlinear losses (γ) over a broad range of magnitudes [Fig. 5(a)], with a ratio $\gamma/K \sim 0.5$ (dashed line and Table I). At the base temperature, the nonlinearity is higher for the samples presenting higher losses in the linear regime [Fig. 5(b)]. K and γ depend strongly on frequency, with $K \sim f^3$–f^4 [dotted lines in Fig. 5(c)] and $\gamma \sim f^{3.5}$–f^5, with $K/\gamma \sim f$. Finally, the temperature dependence of K and γ is measured for two samples [C, shown in Fig. 5(d), and F]. The nonlinearity increases globally with temperature. To explain the nonlinearity characterized here, we examine in detail the two most common sources of nonlinearity in superconducting resonators: the nonlinearity of the kinetic inductance induced by depairing, and the nonlinearity induced by quasiparticle heating.

IX. MODELING NONLINEARITY WITH DEPAIRING

Nonlinear behavior with the rf power is generally expected in superconducting resonators due to the nonlinearity of the kinetic inductance with respect to the current, $L_k = L_{k,0}(1 + I^2/I_\Gamma^2)$, where I_Γ, the depairing current, is of the order of the critical current ($I_\Gamma \sim 1.88 \times I_c$ [39]), and

accounts for the weakening of superconductivity under a phase gradient. Indeed, static depairing (induced by a dc current, a dc magnetic field, or static magnetic impurities) induces closing of the gap and smoothed BCS coherence peaks [39], while the density of states remains strictly zero below the reduced gap, as in Abrikosov-Gorkov-type impurity scattering. In the case of dynamic depairing (induced by an ac current or ac magnetic field), both the density of states and the distribution functions are modified, with, in particular, a nonzero density of states well below the gap [24]. To determine how much the conductivity deviates from the linear response at a certain current I, one has to evaluate the first-order correction to the superconducting gap $\Delta(I)$, and hence to the kinetic inductance $L_k(I)$ in the presence of depairing. For an LC resonator, a relative shift of the frequency is induced by a relative shift of the inductance and is related to the current following

$$\frac{\delta f}{f} = -\frac{\alpha}{2}\frac{\delta L_k}{L_k} = -\frac{\alpha}{2}\frac{I^2}{I_\Gamma^2},$$

which is valid for $I \ll I_\Gamma$. Expressing the energy stored in the inductor in terms of the average number of photons $\bar{n}\hbar\omega = 1/(2\alpha)L_k I^2$ enables one to relate K to the depairing current

$$K_{\text{dep}} = \frac{2\pi\,\delta f}{\bar{n}} \sim -\alpha^2\frac{\hbar\omega^2}{L_k I_\Gamma^2}. \tag{5}$$

To estimate the order of magnitude of K_{dep}, one can calculate I_Γ from the critical current density in Si:B, $j_c \sim 6 \times 10^8$ A/m^2, obtained from dc measurements on wires of identical width, thickness $t = 35$ nm, and length $l = 0.55$ mm. As an example, in the geometry of sample C, we obtain $|K_{\text{dep}}|/2\pi \sim 1$ Hz/photon, more than 2 orders of magnitude smaller than the measured value,

$|K_{\mathrm{meas}}|/2\pi = 230$ Hz/photon. A more accurate expression,

$$K_{\mathrm{dep}} = -\alpha^2 \frac{e^2}{h} \frac{9\pi^2}{4} m^2 \frac{1}{\mathcal{C}_g} \frac{\xi^2}{l^3}, \qquad (6)$$

is derived from the Usadel equations, where m is the mode number, ξ is the superconducting coherence length, and l is the length of the resonator. This expression has been shown to give reliable predictions of the Kerr coefficient for Al, NbSi, TiN, and Nb-Ti-N resonators [40] in a half-wave CPW superconducting resonator. Note that this prediction accounts for static depairing, and not dynamic depairing as described in Ref. [24]. However, it is justified in the limit $hf \ll \Delta$, where our measurements are performed. Indeed, although the density of states is markedly different in the two cases, the conductivities are modified significantly by dynamic depairing only when hf is close to Δ.

The only two varying parameters in Eq. (6) are l and ξ, the geometrical capacitance per unit length $\mathcal{C}_g \sim 150$ pF/m of the CPW being fixed mainly by the substrate dielectric constant and α being near 1 for all our samples. The length l is given by the design and is checked after fabrication, and has an estimated error of about 1% at most. The superconducting coherence length ξ is determined from independent dc magnetotransport measurements for each Si:B layer [36], and is reported in Table I. This quantity is well determined to within a factor of 2. The estimations of $K_{\mathrm{dep}}/2\pi$ from Eq. (6) for all resonators studied are systematically lower than the experimental values by 2–3 orders of magnitude, well outside the error bars on $K_{\mathrm{dep}}/2\pi$ coming from the extraction of material parameters and the spread in the fabrication. Moreover, we expect $|K_{\mathrm{dep}}|/2\pi$ to increase with temperature through the temperature dependence of the superconducting gap, as $K_{\mathrm{dep}}(T) \sim \xi^2 \sim 1/\Delta(T)$, in the dirty limit where $\xi = \sqrt{\hbar D/\Delta}$. This is observed neither in the shape nor in the magnitude of $K(T)$ shown in Fig. 5(d). Indeed, in both samples C and F, between 11 and 150 mK, K increases by 100%, while Δ varies by only 0.5%. The depairing model thus fails to predict the observed Kerr coefficient, which is dominated by another source of nonlinearity.

X. MODELING NONLINEARITY WITH HEATING OF QUASIPARTICLES

Another possible explanation for the observed nonlinearity is heating of the quasiparticle (QP) system by the absorbed microwave power. The quasiparticle system is cooled both by inelastic electron-phonon scattering (whose strength is proportional to the material-dependent parameter Σ_N), as in a normal metal, and by quasiparticle recombination, producing phonons with energies greater than 2Δ that may escape from the layer (whose strength is proportional to the material-dependent parameter Σ_S).

Whenever the microwave power absorbed by the QP system exceeds the cooling power due to electron-phonon scattering and quasiparticle recombination, the effective equilibrium temperature of the QPs increases, reducing both the resonance frequency and the internal quality factor (as seen in Fig. 3). The resulting equilibrium depends on the difference between the microwave frequency and the resonance frequency, as the maximum microwave absorption happens only at resonance. As a consequence, heating leads to skewing and hysteresis in $S_{21}(f)$, as in the case of depairing, and could account for the experimental data shown in Fig. 4(a) (see Appendix). This model is detailed in Ref. [41] for normal-metal electron-phonon cooling, and in Ref. [25,42] for the superconducting case that we consider here.

Assuming the extreme scenario where all the missing power at the output port of the resonator is dissipated by QPs, we compute the expected frequency shift as a function of the number of photons, deriving the "apparent" Kerr and nonlinear loss coefficients.

As ultradoped silicon is a little-known material, we adjust the value of $\Sigma_S \propto \Delta^4 \Sigma_N$ [42] to best reproduce the measured Kerr coefficient for each mode, assuming a thermal quasiparticle distribution. The values obtained are in the range $\Sigma_S = (0.02\text{–}20)$ nW μm^{-3} K^{-1}, with a mean around $\Sigma_S = 1$ nW μm^{-3} K^{-1}, giving an unexpectedly large spread for nominally identical samples, some of them even fabricated and measured simultaneously. A theoretical lower limit on Σ_S can be estimated from the value of $\Sigma_N = 0.05$ nW μm^{-3} K^{-5} for a Si:B film of smaller concentration, 5×10^{20} cm^{-3} [43]. We find $\Sigma_S = 0.02$ nW μm^{-3} K^{-1}, almost 2 orders of magnitude smaller than what we extract from most of our measurements. We would thus naively expect a much higher heating (and nonlinearity) than what we observe. This implies that, at low temperature, we cannot rule out the contribution of heating to the nonlinearity in Si:B. However, both the Kerr amplitude and the nonlinear losses induced by heating are expected to decrease when the temperature increases, as the cooling becomes more efficient with an increase in the phonon population. This qualitative argument should hold also for a nonequilibrium nonthermal distribution function with an excess of QPs [44]. However, the exact opposite is observed in Fig. 5(d). In addition, the expected ratio $\gamma_{\mathrm{th}}/K_{\mathrm{th}}$ for heating at equilibrium, $\gamma_{\mathrm{th}}/K_{\mathrm{th}} = 0.85$, is approximately double the measured value. In conclusion, while we do not exclude quasiparticle heating at the lowest temperatures, another mechanism is dominant for higher temperatures above 100 mK.

XI. OTHER POSSIBLE SOURCES OF NONLINEARITY

The correlation of linear and nonlinear losses with the Kerr term suggests that the mechanism at the root of the

nonlinearity that we observe in Si:B must comprise energy dissipation and heating of the system, and might also be responsible for the saturation of the internal losses in the linear regime. In addition to possible quasiparticle heating at the lowest temperatures, we suggest another nonlinear mechanism that might induce a change in both the frequency and the dissipation, related to the two-dimensional (2D) nature of the superconducting layer. As the Si:B resonator is thinner than the coherence length, vortex-antivortex bound pairs are present even in the absence of any magnetic field, pinned to material defects. We consider here the situation in our experiment where the induced ac magnetic field in the resonator is not strong enough to enable vortices to enter the superconductor. These vortex-antivortex pairs, whose number and depinning increase with the amplitude of the ac bias, modify the current lines circulating in the superconductor, and can induce a strong nonlinearity both in the reactive and in the dissipative response, as was shown for the extreme case of a granular superconductor modeled as a Josephson-junction network [45]. In our case, even though Si:B is not a granular material, the variations of the gap due to doping modulations may induce an array of Dayem weak links, qualitatively described by the same physics. When the temperature or the current increases, the bound states progressively dissociate, inducing a strong increase in the dissipation nonlinearity. To further test this hypothesis, we plan to perform experiments in a magnetic field and with engineered flux traps in the inner conductor of the CPW, but such experiments are beyond the scope of the present work.

XII. CONCLUSION

In this paper, we demonstrate resonating microwave circuits made from superconducting silicon. They are realized in laser-ultradoped Si:B layers with standard microelectronics processes. Si:B presents a large kinetic inductance, in agreement with BCS expectations and in the range from 50 to 470 pH/$\square$, comparable to the values for strongly disordered superconductors. The temperature dependence of the kinetic inductance up to $0.6 T/T_c$ is similarly well understood in the framework of the Mattis-Bardeen theory, with no adjustable parameters. The internal losses at high temperature ($T/T_c > 0.3$) are also well described by the Mattis-Bardeen theory as being due to thermally activated quasiparticles. However, at low temperature, the internal losses saturate, limiting the quality factor to a few thousand, possibly due to the contribution of vortex-induced dissipation. When the readout power is increased, we find evidence of an unexpectedly strong nonlinearity in the kinetic inductance and the losses, 2 orders of magnitude larger than that predicted for depairing. The observed nonlinearity increases with temperature, a dependence that is at odds with a quasiparticle-heating model. We speculate

that this strong nonlinearity is related to the 2D geometry of our superconducting silicon films. The work presented here opens up the possibility of using Si:B in superconducting circuits on a quantum silicon platform, once its properties are optimized through a better understanding of the origins of the losses and of the large nonlinearity.

APPENDIX

1. Laser doping

The doping is performed in an ultrahigh-vacuum chamber (pressure 1×10^{-9} mbar), where a puff of the precursor gas BCl_3 is injected onto the p-type (100) Si sample surface. The substrate is then melted with a 25-ns ultraviolet pulse generated by an excimer XeCl laser. The boron diffuses into the liquid silicon and is incorporated substitutionally during fast epitaxy (the recrystallization velocity is about 4 m/s), while the Cl creates volatile compounds with the atoms in the first atomic layers, resulting in a cleaner sample surface. With our GILD setup, we observe that the maximum active doping boron density saturates at around 4.7×10^{21} cm^{-3}, the density being possibly limited by the pulse duration. The layers studied in this paper are near such saturation. Close to the saturation concentration, the boron activation is impaired, and the ratio of interstitial boron to substitutional boron is increased. This effect is particularly evident for the thinner layers, where this saturation happens sooner, leading to more interstitial boron and more disorder.

2. Silicon-resonator design

The practical implementation of the coupling to the input line differs for the two geometries. In the "transmission" coupled resonator, one can easily tune Q_c from about 1×10^2 to 1×10^6 by adjusting the input and output coupling capacitors. For moderately low values of Q_c such as the ones targeted here, we implement this coupling using interdigitated capacitors that have 30-μm-long fingers and a 4-μm spacing. In the "shunt" coupling scheme, one generally tunes Q_c with the length of the resonator conductor running along the transmission line [see Fig. 1(b)]. In that case, to obtain values of $Q_c \sim 3000$, the coupling length may reach a few millimeters, comparable to the resonator

length. This results in less well-controlled coupling quality factors for the higher harmonics of the resonator.

Note that the "shunt" geometry has the advantage over the "transmission" geometry that it enables extracting both Q_c and Q_i as independent parameters from a single measurement. This is simply because the out-of-resonance signal provides a calibration of the measurement acquisition chain, while in the "transmission" scheme, one has to calibrate the setup in a separate measurement, or rely on microwave simulation for a knowledge of Q_c. Note that for the "shunt" coupled geometry the fitted Q_c values are always within 10% of the simulated values, which gives us confidence in the reliability of the values of Q_c used for the "transmission" geometry.

3. Extraction of the sheet kinetic inductance

The analytical expression for the resonance frequency of the first harmonic reads $f_1 = 1/pl\sqrt{\mathcal{C}_g(\mathcal{L}_g + \mathcal{L}_k)}$, where l is the length of the resonator, and $p = 2$ for a half-wave resonator and $p = 4$ for a quarter-wave resonator. The geometrical capacitance and inductance per unit length, $\mathcal{C}_g$ (~ 150 pF/m) and $\mathcal{L}_g$ (~ 500 nH/m), are found from standard analytical expressions using the CPW width w and gap s [see Fig. 1(e)], and the dielectric constant of the Si substrate. The sheet kinetic inductance $L_{k,\square}$ is calculated from the kinetic inductance per unit length as $\mathcal{L}_k = g_c L_{k,\square}^{\text{SiB}} + g_g L_{k,\square}^{\text{Al}}$, where g_c and g_g are geometrical factors, which are derived, e.g., in Ref. [31] by integrating over current distributions in the CPW. In our case, $\mathcal{L}_k \approx g_c L_{k,\square}^{\text{SiB}}$, since the sheet kinetic inductance of an Al film is much smaller than that of a Si:B one.

4. Measurement setup and linear response

We perform the measurements in a cryogen-free dilution refrigerator, with the temperature T_{base} of the cold stage regulated between 12 mK and 2 K. A 1–12-GHz signal generated by a vector network analyzer (VNA) is attenuated by 90–110 dB (depending on the experiment) by both room-temperature and cold attenuators before reaching the sample. The incoming power in the sample is known to 1 dB from a separate calibration of the input line. The signal leaving the sample is amplified by an amplifier chain with a total gain of approximately 107 dB and then fed to the input port of the VNA. The first-stage HEMT amplifier, anchored at 4 K, has a gain of 32 dB and a noise temperature $T_N \sim 9$ K at 3 GHz. To protect the Si:B resonators from thermal radiation from the HEMT, either a 3–12-GHz isolator or an attenuator is anchored to the coldest stage between the sample and the HEMT.

In order to reach thermal equilibrium during the temperature ramp, at each temperature step the mixing-chamber temperature is regulated by use of the indication of a thermometer anchored to the sample, and the sample is allowed to thermalize for 10–15 min before data acquisition is started. At all temperatures, we use the highest admissible power to maintain a linear response while improving the signal-to-noise ratio.

5. Losses from magnetic vortices

It is possible to estimate the complex resistivity associated with vortex motion,

$$\rho_v = \rho_n \frac{B - B_{\text{th}}}{B_{c,2}} \frac{if/f_d}{1 + if/f_d}, \tag{A1}$$

where $\rho_n \sim 10^{-4}$ Ω cm is the normal-state resistivity of the Si:B, $B_{c,2} \sim 0.1$ T is the upper critical field, and f_d is the characteristic depinning frequency [46,47]. B_{th} is the threshold magnetic field for vortex generation, which scales with the width of the Si:B line as $B_{\text{th}} \sim \Phi_0/w^2$, giving $B_{\text{th}} \sim 0.8$ G for $w = 5$ μm (sample C). This threshold is about 3 orders of magnitude higher than the microwave-induced magnetic field; however, vortices can be present due to imperfect magnetic screening of the sample. For frequencies smaller than f_d, the real, dissipative, part of the complex resistivity goes as $\rho_v \sim f^2$, as qualitatively observed in Fig. 2(g). Moreover, quantitative agreement can be obtained with Eq. (A1). The depinning frequency calculated from the experimental dc parameters is $f_d = \rho_n j_c / 2\pi \xi B_{c,2} = 19$ GHz, where $j_c \sim 6 \times 10^8$ A/m^2 is the measured critical current density. The threshold magnetic field is taken as $B_{\text{th}} = \Phi_0/w^2$. To interpret the measurements within this model, we need to assume the presence of a stray 1–2-G magnetic field.

6. Nonlinear response: Resolution of the nonlinear Hamiltonian

The steady-state equation for the electromagnetic energy inside the resonator is a third-order polynomial that depends on the incident power, the frequency, and the losses. This polynomial allows between one and three real roots, which are used to compute the forward-scattering parameter $S_{21}(f)$. Note that when there exist three real solutions for the energy, one corresponds to a low amplitude, one to a high amplitude, and the third to a metastable state not accessible experimentally. The two accessible states describe the hysteretic regime, and are accessed depending on the history (e.g., a frequency sweep up or down).

The presence of multiple harmonics in our resonators allows us to follow the evolution of K and γ with the frequency in the same device.

7. Quasiparticle-heating model

The power dissipated by the QPs, $P_{\text{QP}} = \bar{n}\hbar\omega_r\chi\kappa_i$, is proportional to the energy stored in the resonator, $\bar{n}\hbar\omega_r$, and to $\chi\kappa_i$, the energy loss rate due to quasiparticles, where

$0 \leq \chi \leq 1$. Thus, $P_{QP} = (2P_{in}\chi\kappa_c\kappa_i/\kappa_t^2)[1 + (2\delta\omega/\kappa_t)^2]$ is maximum at resonance ($\delta\omega = 0$) and for critical coupling ($\kappa_c = \kappa_i$). After fixing χ, one finds the equilibrium temperature by equating P_{QP} with the quasiparticle-phonon power flow, given by the recombination term, which is proportional to the material-dependent Σ_s, and the scattering term, proportional to Σ_n [42]. From the equilibrium temperature, the resonance frequency and internal quality factor are found as a function of microwave power, which enables the apparent "Kerr constant" $\partial f_r/\overline{n}$ to be computed.

[1] N. Samkharadze, A. Bruno, P. Scarlino, G. Zheng, D. P. DiVincenzo, L. DiCarlo, and L. M. K. Vandersypen, High-Kinetic-Inductance Superconducting Nanowire Resonators for Circuit QED in a Magnetic Field, Phys. Rev. Appl. **5,** 044004 (2016).

[2] R. Kuzmin, R. Mencia, N. Grabon, N. Mehta, Y.-H. Lin, and V. E. Manucharyan, Quantum electrodynamics of a superconductor–insulator phase transition, Nat. Phys. **15,** 930 (2019).

[3] S. Léger, J. Puertas-Martínez, K. Bharadwaj, R. Dassonneville, J. Delaforce, F. Foroughi, V. Milchakov, L. Planat, O. Buisson, C. Naud, W. Hasch-Guichard, S. Florens, I. Snyman, and N. Roch, Observation of quantum many-body effects due to zero point fluctuations in superconducting circuits, Nat. Commun. **10,** 1 (2019).

[4] V. E. Manucharyan, J. Koch, L. I. Glazman, and M. H. Devoret, Fluxonium: Single cooper-pair circuit free of charge offsets, Science **326,** 113 (2009).

[5] S. P. Harvey, C. G. L. Bøttcher, L. A. Orona, S. D. Bartlett, A. C. Doherty, and A. Yacoby, Coupling two spin qubits with a high-impedance resonator, Phys. Rev. B **97,** 235409 (2018).

[6] P. K. Day, H. G. LeDuc, B. A. Mazin, A. Vayonakis, and J. Zmuidzinas, A broadband superconducting detector suitable for use in large arrays, Nature **425,** 817 (2003).

[7] R. Barends, J. J. A. Baselmans, J. N. Hovenier, J. R. Gao, S. J. C. Yates, T. M. Klapwijk, and H. F. C. Hoevers, Niobium and tantalum high Q resonators for photon detectors, IEEE Trans. Appl. Supercond. **17,** 263 (2007).

[8] J. Zmuidzinas, Superconducting microresonators: Physics and applications, Annu. Rev. Cond. Matter Phys. **3,** 169 (2012).

[9] R. Maurand, X. Jehl, D. Kotekar-Patil, A. Corna, H. Bohuslavskyi, R. Laviéville, L. Hutin, S. Barraud, M. Vinet, M. Sanquer, and S. De Franceschi, A CMOS silicon spin qubit, Nat. Commun. **7,** 13575 (2016).

[10] E. Bustarret, C. Marcenat, P. Achatz, J. Kačmarčik, F. Lévy, A. Huxley, L. Ortéga, E. Bourgeois, X. Blase, D. Débarre, and J. Boulmer, Superconductivity in doped cubic silicon, Nature **444,** 465 (2006).

[11] C. Marcenat, J. Kačmarčik, R. Piquerel, P. Achatz, G. Prudon, C. Dubois, B. Gautier, J. C. Dupuy, E. Bustarret, L. Ortéga, T. Klein, J. Boulmer, T. Kociniewski, and D. Débarre, Low-temperature transition to a superconducting phase in boron-doped silicon films grown on (001)-oriented silicon wafers, Phys. Rev. B **81,** 020501 (2010).

[12] A. Bhaduri, T. Kociniewski, F. Fossard, J. Boulmer, and D. Débarre, Optical and electrical properties of laser doped Si:B in the alloy range, Appl. Surf. Sci. **258,** 9228 (2012).

[13] A. Grockowiak, T. Klein, E. Bustarret, J. Kačmarčík, C. Dubois, G. Prudon, K. Hoummada, D. Mangelinck, T. Kociniewski, D. Débarre, J. Boulmer, and C. Marcenat, Superconducting properties of laser annealed implanted Si:B epilayers, Supercond. Sci. Technol. **26,** 045009 (2013).

[14] L. J. Swenson, P. K. Day, B. H. Eom, H. G. Leduc, N. Llombart, C. M. McKenney, O. Noroozian, and J. Zmuidzinas, Operation of a titanium nitride superconducting microresonator detector in the nonlinear regime, J. Appl. Phys. **113,** 104501 (2013).

[15] H. G. Leduc, B. Bumble, P. K. Day, B. H. Eom, J. Gao, S. Golwala, B. A. Mazin, S. McHugh, A. Merrill, D. C. Moore, O. Noroozian, A. D. Turner, and J. Zmuidzinas, Titanium nitride films for ultrasensitive microresonator detectors, Appl. Phys. Lett. **97,** 102509 (2010).

[16] A. Shearrow, G. Koolstra, S. J. Whiteley, N. Earnest, P. S. Barry, F. J. Heremans, D. D. Awschalom, E. Shirokoff, and D. I. Schuster, Atomic layer deposition of titanium nitride for quantum circuits, Appl. Phys. Lett. **113,** 212601 (2018).

[17] A. J. Annunziata, D. F. Santavicca, L. Frunzio, G. Catelani, M. J. Rooks, A. Frydman, and D. E. Prober, Tunable superconducting nanoinductors, Nanotechnology **21,** 445202 (2010).

[18] D. Niepce, J. Burnett, and J. Bylander, High Kinetic Inductance NbN Nanowire Superinductors, Phys. Rev. Appl. **11,** 044014 (2019).

[19] J. R. Gao, M. Hajenius, F. D. Tichelaar, T. M. Klapwijk, B. Voronov, E. Grishin, G. Gol'tsman, C. A. Zorman, and M. Mehregany, Monocrystalline NbN nanofilms on a 3C-SiC/Si substrate, Appl. Phys. Lett. **91,** 062504 (2007).

[20] J. D. McCambridge, *The Superconducting Properties of Niobium-Titanium Alloy Multilayers.* PhD thesis, 1995.

[21] M. Calvo, A. D'Addabbo, A. Monfardini, A. Benoit, N. Boudou, O. Bourrion, A. Catalano, L. Dumoulin, J. Goupy, H. le Sueur, and S. Marnieros, Niobium silicon alloys for kinetic inductance detectors, J. Low Temp. Phys. **176,** 518 (2014).

[22] J. Basset, D. Watfa, G. Aiello, M. Féchant, A. Morvan, J. Estève, J. Gabelli, M. Aprili, R. Weil, A. Kasumov, H. Bouchiat, and R. Deblock, High kinetic inductance microwave resonators made by He-Beam assisted deposition of tungsten nanowires, Appl. Phys. Lett. **114,** 102601 (2019).

[23] N. Maleeva, L. Grünhaupt, T. Klein, F. Lévy-Bertrand, O. Dupre, M. Calvo, F. Valenti, P. Winkel, F. Friedrich, W. Wernsdorfer, A. V. Ustinov, H. Rotzinger, A. Monfardini, M. V. Fistul, and I. M. Pop, Circuit quantum electrodynamics of granular aluminum resonators, Nat. Commun. **9,** 26 (2018).

[24] A. V. Semenov, I. A. Devyatov, P. J. de Visser, and T. M. Klapwijk, Coherent Excited States in Superconductors due to a Microwave Field, Phys. Rev. Lett. **117,** 445 (2016).

[25] T. Guruswamy, D. J. Goldie, and S. Withington, Nonequilibrium superconducting thin films with sub-gap and

pair-breaking photon illumination, Supercond. Sci. Technol. **28,** 054002 (2015).

[26] F. Chiodi, R. Daubriac, and S. Kerdilès, *Chapter 9 - Laser ultra-doped silicon: Superconductivity and applications*. Woodhead Publishing Series in Electronic and Optical Materials, Woodhead Publishing, 2021.

[27] F. Dahlem, T. Kociniewski, C. Marcenat, A. Grockowiak, L. M. A. Pascal, P. Achatz, J. Boulmer, D. Débarre, T. Klein, E. Bustarret, and H. Courtois, Subkelvin tunneling spectroscopy showing bardeen-cooper-Schrieffer superconductivity in heavily boron-doped silicon epilayers, Phys. Rev. B **82,** 140505 (2010).

[28] A. J. Murrell, E. J. H. Collart, M. A. Foad, and D. Jennings, Process interactions between low-energy ion implantation and rapid-thermal annealing for optimized ultrashallow junction formation, J. Vacuum Sci. Technol. B: Microelectron. Nanometer Struct. Process., Meas., Phenom. **18,** 462 (2000).

[29] D. Débarre, G. Kerrien, T. Noguchi, and J. Boulmer, Laser doping for ultra-shallow junctions monitored by time resolved optical measurements, IEICE Trans. Electron. **E85-C,** 1098 (2002).

[30] K. Hoummada, F. Dahlem, T. Kociniewski, J. Boulmer, C. Dubois, G. Prudon, E. Bustarret, H. Courtois, D. Débarre, and D. Mangelinck, Absence of boron aggregates in superconducting silicon confirmed by atom probe tomography, Appl. Phys. Lett. **101,** 182602 (2012).

[31] J. Gao, *The Physics of Superconducting Microwave Resonators*. PhD thesis, California Institute of Technology, June 2008.

[32] G. Stan, S. B. Field, and J. M. Martinis, Critical Field for Complete Vortex Expulsion from Narrow Superconducting Strips, Phys. Rev. Lett. **92,** 097003 (2004).

[33] M. S. Khalil, M. J. A. Stoutimore, F. C. Wellstood, and K. D. Osborn, An analysis method for asymmetric resonator transmission applied to superconducting devices, J. Appl. Phys. **111,** 054510 (2012).

[34] A. Megrant, C. Neill, R. Barends, B. Chiaro, Y. Chen, L. Feigl, J. Kelly, E. Lucero, M. Mariantoni, P. J. J. O'Malley, D. Sank, A. Vainsencher, J. Wenner, T. C. White, Y. Yin, J. Zhao, C. J. Palmstrøm, J. M. Martinis, and A. N. Cleland, Planar superconducting resonators with internal quality factors above one million, Appl. Phys. Lett. **100,** 113510 (2012).

[35] L. Faoro and L. B. Ioffe, Interacting tunneling model for two-level systems in amorphous materials and its predictions for their dephasing and noise in superconducting microresonators, Phys. Rev. B **91,** 936 (2015).

[36] P. Bonnet, *Mesures résonantes des propriétés hautes fréquences du silicium supraconducteur ultra-dopé au bore par laser.* PhD thesis, 2019.

[37] D. C. Mattis and J. Bardeen, Theory of the anomalous skin effect in normal and superconducting metals, Phys. Rev. **111,** 412 (1958).

[38] B. Yurke and E. Buks, Performance of cavity-parametric amplifiers, employing kerr nonlinearites, in the presence of two-photon loss, J. Lightwave Technol. **24,** 5054 (2006).

[39] A. Anthore, H. Pothier, and D. Esteve, Density of States in a Superconductor Carrying a Supercurrent, Phys. Rev. Lett. **90,** 599 (2003).

[40] N. Bourlet, A. Murani, P. Joyez, and H. le Sueur, unpublished calculation, 2021.

[41] D. J. Goldie and S. Withington, Non-equilibrium superconductivity in quantum-sensing superconducting resonators, Supercond. Sci. Technol. **26,** 015004 (2012).

[42] T. Guruswamy, *Nonequilibrium behaviour and quasiparticle heating in thin film superconducting microwave resonators*. PhD thesis, Department of Physics, University of Cambridge, 2018.

[43] F. Chiodi, J. E. Duvauchelle, C. Marcenat, D. Débarre, and F. Lefloch, Proximity-induced superconductivity in all-silicon superconductor /normal-metal junctions, Phys. Rev. B **96,** 342 (2017).

[44] P. J. de Visser, D. J. Goldie, P. Diener, S. Withington, J. J. A. Baselmans, and T. M. Klapwijk, Evidence of a Nonequilibrium Distribution of Quasiparticles in the Microwave Response of a Superconducting Aluminum Resonator, Phys. Rev. Lett. **112,** 047004 (2014).

[45] T. Dalim and J. Oppenlander, Vortex pairs and nonlinear inductance of high-tc superconducting microwave resonators, IEEE Trans. Appl. Supercond. **II,** 1392 (2001).

[46] J. I. Gittleman and B. Rosenblum, The pinning potential and high-frequency studies of type-ii superconductors, J. Appl. Phys. **39,** 2617 (1968).

[47] C. Song, T. W. Heitmann, M. P. DeFeo, K. Yu, R. McDermott, M. Neeley, J. M. Martinis, and B. L. T. Plourde, Microwave response of vortices in superconducting thin films of Re and Al, Phys. Rev. B **79,** 174512 (2009).